

***Ab initio* synthesis of single-layer III-V materials**

Arunima K. Singh, Houlong L. Zhuang, and Richard G. Hennig*

Department of Materials Science and Engineering, Cornell University, Ithaca, New York 14853, USA

(Received 14 February 2014; revised manuscript received 4 June 2014; published 19 June 2014)

The discovery of a novel material requires the identification of the material's composition as well as of suitable synthesis conditions. We present a data-mining approach to identify suitable substrates for the growth of two-dimensional materials and apply the method to the recently predicted two-dimensional III-V compounds. We identify several lattice-matched substrates for their epitaxial growth, stabilization, and functionalization. Density-functional calculations show that these substrates sufficiently reduce the formation energies of the metastable two-dimensional materials to make them thermodynamically stable. We show that chemical interactions of the two-dimensional materials with the substrates shift the Fermi level of these materials, resulting in doping. The large adsorption energies and strong doping indicate that these metals should provide good electrical contact to enable transport measurements and electronic applications.

DOI: [10.1103/PhysRevB.89.245431](https://doi.org/10.1103/PhysRevB.89.245431)

PACS number(s): 68.43.-h, 73.22.-f, 71.15.Mb, 73.61.Ey

I. INTRODUCTION

Since the first experiments on freestanding single-layer graphene [1,2], this remarkable two-dimensional (2D) material has attracted great scientific interest [3] and paved the way for the discovery and synthesis of many other 2D materials [4–11]. 2D materials present a whole new class of materials whose properties differ from those of their three-dimensional (3D) counterparts. Examples of successfully synthesized 2D materials include BN, MoS₂, ZnO, SnS₂, and WSe₂ [5–7,12,13]. While several 2D materials have been discovered in experiments, the recently predicted 2D III-V materials are a new addition to the field awaiting to be synthesized [8,9].

In two recent studies, we identified a large number of 2D materials in the group III-V family [8,9]. These 2D materials are metastable with formation energies ranging from 0.1 to 1 eV/atom. The 2D materials can exhibit a honeycomb hexagonal structure that is either planar or buckled as illustrated in Fig. 4(b). In addition to these hexagonal structures, we identified a previously unknown low-energy tetragonal structure that is shown in Fig. 4(a). For several of the 2D III-V materials, the tetragonal structure is lower in energy than the hexagonal one. The electronic properties of these materials range from metallic to semiconducting with band gaps spanning the range of visible light, making these 2D materials promising candidates for nanoelectronic applications.

We envision the synthesis of the newly discovered 2D III-V materials via methods commonly employed for other 2D materials such as graphene, BN, MoS₂, etc. Chemical vapor deposition and molecular beam epitaxy are among probably a dozen methods being developed and used to prepare graphene of various dimensions, shapes, and quality [4,14–17]. These and other synthesis methods for 2D materials require suitable substrates. The synthesis on substrates is an ideal processing technique for 2D materials because it can produce high-quality, large-area, and low-defect samples with reasonable yields and relatively low production costs. In comparison, another widely

used method of synthesis of graphene, mechanical exfoliation, provides excellent quality samples but lacks in scalability.

In this paper, we identify suitable substrates for the stabilization of the 2D III-V materials, thereby providing epitaxial synthesis routes for the growth of these promising materials. For each 2D III-V material in the hexagonal and tetragonal structure we select symmetry and lattice-matched high atomic density surfaces of transition-metal and rare-earth-metal substrates and subsequently calculate their energetic stabilization on these substrates. We further determine how the substrates affect the structural and electronic properties of the 2D III-V materials. We find several substrates that can energetically stabilize these materials and show that chemical interactions of the 2D materials with the substrates shift their Fermi level, resulting in charge transfer and doping of the 2D materials. Beyond their role as substrates, the metals can also be employed as electrical contacts for these 2D materials for electronic transport measurements and applications in electronic devices. The observed large adsorption energies and strong doping indicate that the metals studied in this work should provide good electrical contact.

II. SIMULATION METHODS

All calculations are based on density-functional theory (DFT) using the projector-augmented wave method as implemented in the plane-wave code VASP [18–20]. An energy cutoff of 400 eV and a $6 \times 6 \times 1$ k -point mesh result in an accuracy for the binding energies of 3 meV/atom for the 2D material. For the calculation of the elastic constants, we increase the cutoff energy to 700 eV for an accuracy of about 1 N/m. After full structural optimization, a denser k -point grid of $20 \times 20 \times 1$ is employed in the calculation of the electronic properties. DFT calculations of the adsorption energies are performed using a slab geometry with a vacuum spacing of 18 Å, which ensures that the interactions between the layers are negligible. The generalized gradient approximation with the Perdew-Burke-Ernzerhof (PBE) parametrization is used for most calculations unless mentioned otherwise. The van der Waals interactions between the 2D materials and substrates are modeled using the vdW-DF functional with the optB88 exchange functional [21].

*rhennig@cornell.edu

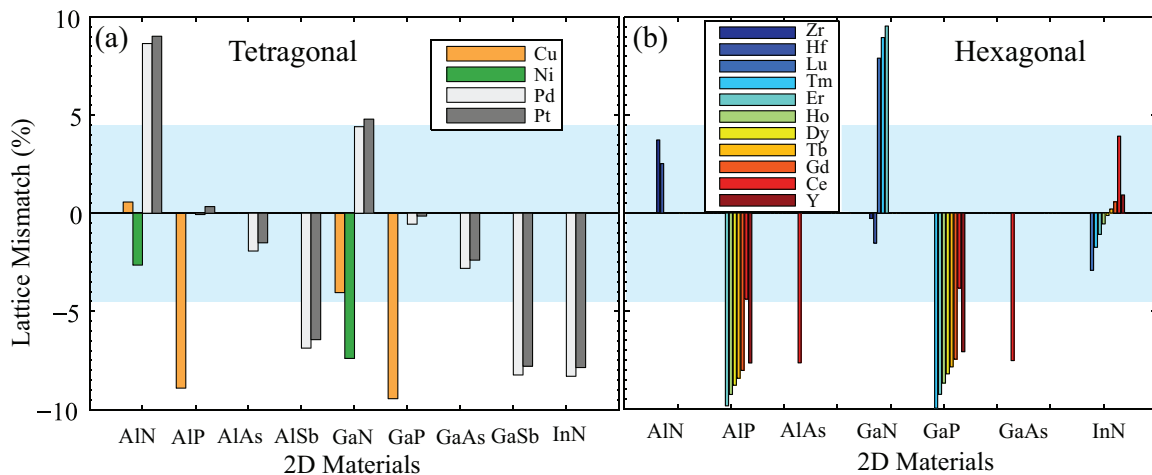


FIG. 1. (Color online) Lattice mismatch (a) for the 2D tetragonal III-V materials and the (100) surfaces of transition metals and (b) for the 2D hexagonal III-V materials and the (0001) surfaces of hcp transition and rare-earth metals. The values for the lattice mismatches are provided in the Supplemental Material [29].

The fcc and hcp transition- and rare-earth-metal surfaces are modeled as slabs consisting of eight and nine layers, respectively; the atoms in the bottom three layers are fixed to their bulk positions. While Pt(100) surface shows a hexagonal large-scale reconstructed surface structure [22], we model the unreconstructed Pt(100) surface for simplicity and also because the reconstruction has been shown to be lifted by exposure to gases such as CO_2 , O_2 , H_2 , C_2H_4 [23–26]. The 2D materials are strained appropriately to match the lattices of the substrates as illustrated in Fig. 1.

III. SUBSTRATE CHOICES

Common substrates used for the synthesis of graphene and single-layer boron nitride encompass transition metals, silicon carbide, sapphire, tantalum carbide, silicon dioxide, metal nitrides, etc. [27]. In particular, the metal surfaces efficiently catalyze the chemical vapor deposition process and stabilize graphene. The metal substrates also provide high-symmetry facets with high atomic density facets such as (111), (110), (100), and (0001) surfaces which are ideal to produce 2D materials of high quality. Additionally, their prior presence in laboratories and hence easy access is an attractive reason for utilizing them to grow the 2D III-V materials.

For epitaxial growth, the potential substrate surfaces should exhibit the same symmetry as the 2D materials (hexagonal or tetragonal). For the hexagonal 2D materials, this leads to substrate surfaces that are either (111) surfaces of cubic materials or (0001) surfaces of hexagonal ones. For the tetragonal 2D materials, this means that (100) surfaces of cubic materials provide a match.

In addition to the symmetry matching of the 2D materials and substrates, it is crucial for their lattice parameters to be matched as close as possible. This enhances the adsorption energy of the 2D materials on the substrates due to the reduced strain energy of the 2D materials. The lattice matching could include direct matches (1:1, 1:2, 2:3, etc.), rotations ($1:\sqrt{2}$, etc.), or more complex Moiré patterns. While nonepitaxial

growth can also reduce the formation energy for lattice-mismatched systems [15], we focus in this work only on epitaxial growth to provide a first set of suitable substrates for the 2D materials synthesis.

A search of the Inorganic Crystal Structure Database [28] reveals that fcc and hcp transition metals as well as hcp rare-earth metals are good candidates for epitaxial substrates for the 2D III-V materials with low lattice mismatches as shown in Fig. 1. DFT lattice parameters are used to compute these lattice mismatches. We neglect zero-point vibration and thermal expansion in our estimate of the lattice mismatch as these estimates only change for room temperature by a few percent at most, meaning that the numbers in the Fig. 1 may change by up to ± 1 . Figure 1(a) shows the computed lattice mismatches between the 12 tetragonal 2D III-V materials and the (100) surfaces of Cu, Ni, Pt, and Pd substrates. Figure 1(b) shows the computed lattice mismatches between the hexagonal 2D III-V materials and the (0001) surfaces of hcp transition and rare-earth metals considered as substrates.

To estimate the range of lattice mismatch feasible for epitaxial growth, we determine when the elastic strain energy penalty required for the 2D materials becomes comparable to the desired stabilization energy. We find that the elastic constants of all 2D III-V materials are considerably softer than the values of graphene and 2D boron nitride, allowing for potentially larger epitaxial strains (see Supplemental Material [29]). We observe that the planar hexagonal III-V materials (AlN, AlP, GaN, and InN) are much stiffer than the buckled hexagonal ones. Furthermore, most III-V materials are softest in the tetragonal structure. This trend can be explained by the larger out-of-plane buckling of the tetragonal structure compared to the buckled hexagonal structure [8].

Figure 2 illustrates the energy cost E_{strain} to biaxially strain four of the 2D materials with C_{11} ranging from 38–98 N/m. The resulting strain energy cost is less than 150 meV/atom for compressive and tensile strains up to 4%. Based on these findings, we argue that a lattice mismatch of $\pm 4\%$ provides a reasonable upper bound for epitaxial growth of these 2D materials on substrates. Thus, we consider the

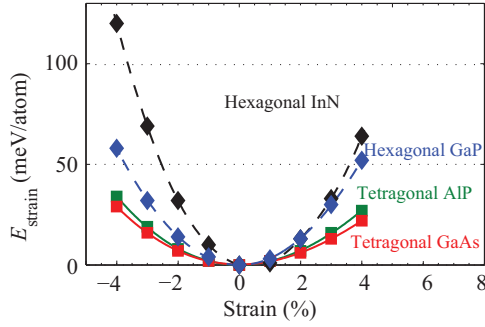


FIG. 2. (Color online) Energy cost E_{strain} for straining the 2D III-V materials with respect to the ground-state structure. The energy cost to strain these materials by $\pm 4\%$ is less than 150 meV/atom.

material combinations shaded in blue in Fig. 1 for the study of adsorption energies.

IV. RESULTS AND DISCUSSION

A. Adsorption configurations

We first identify possible adsorption configurations for the 2D materials on the substrates and then calculate the respective binding energies. Figures 3(a) and 3(b) illustrate possible adsorption sites for atoms on the (0001) surface of hcp and the (100) surface of fcc materials, respectively.

The (0001) surfaces of the hcp transition and rare-earth metals have three possible high-symmetry sites for the atoms of the 2D hexagonal materials, namely, the top, fcc, and hcp sites shown in Fig. 3(a). Since there are two species, group-III atom and group-V atoms, to be adsorbed and there are three sites, there are six possible high-symmetry configurations of hexagonal III-V materials on the (0001) hcp metal surfaces. Additionally, we also placed the hexagonal 2D materials in one low-symmetry configuration on the substrates. We find that the hexagonal 2D III-V materials are most stable in the top(V)-fcc(III) configuration on hcp transition- and rare-earth-metal substrates, illustrated in Fig. 4(b). This is similar to the geometries observed in the adsorption of BN on Cu(111), Ni(111), and Co(0001) [30,31]. In the case of BN, the preferred location of the group-III and group-V elements is similar to the other hexagonal III-V materials. In BN, the group-V element

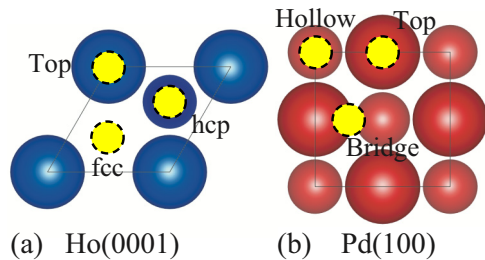


FIG. 3. (Color online) (a), (b) show the schematic representation (top view) of the different possible adsorption sites on Ho(0001) and Pd(100) surfaces, respectively. The large spheres represent the metal atoms in the topmost and the smaller spheres represent the atoms in second to topmost layer. Sites on each metal surface are marked by yellow spheres.

N resides on top of the surface metal atoms and the group-III element B in the fcc hollow site [30,31]. The binding energy of the hexagonal 2D materials adsorbed in the top(V)-hcp(III) configurations is similar to the most stable configurations, for example, InN on Ho in the top(V)-hcp(III) configuration has a binding energy of 0.73 eV/atom, close to the binding energy of 0.75 eV/atom for the top(V)-fcc(III) configuration. The other configurations are typically much weaker bound to the substrate. For example, InN on Ho in the fcc(V)-hcp(III) has a binding energy of only 0.11 eV/atom.

The (100) surfaces of the fcc transition metals also have three possible high-symmetry sites for the atoms of the 2D tetragonal III-V materials, namely, the fourfold top, fourfold hollow, and twofold bridge sites shown in Fig. 3(b). Placing the group-III atoms of the 2D tetragonal materials on these sites leads to three high-symmetry configurations. We calculate the binding energy of the tetragonal III-V materials for these three configurations and a nonsymmetric configuration, where all the atoms of the 2D materials are shifted off the high symmetry sites. We find that the tetragonal materials adsorbed on Pt(100) and Pd(100) surface are most stable in the hollow(III)-top(V) configuration and on Cu(100) and Ni(100) in the top(III)-hollow(V) configuration. All following results are focused on the most stable configurations unless mentioned otherwise.

In our previous work [8], we studied the top(III)-hollow(V) configurations of tetragonal materials adsorbed on Cu, Pd, and Pt (100) substrates. We reported that GaP and AlP are stable in this configuration on Pt and Pd substrates. Here, we consider also two other high-symmetry configurations of the tetragonal 2D materials adsorbed on fcc transition-metal substrates. We find that GaP and AlP are even more stable in the hollow(III)-top(V) configuration.

B. Formation energy

Figure 4 illustrates the stabilization of the 2D materials on the metal substrates. The formation energies of the isolated 2D materials with respect to their 3D structures, $E_{\text{vac}}^{\text{f}} = E_{2\text{D}}/N_{2\text{D}} - E_{3\text{D}}/N_{3\text{D}}$, are reduced by the binding energies of the 2D materials on the substrates E_{b} . The binding energy, E_{b} , is given by

$$E_{\text{b}} = \frac{E_{\text{S}} + E_{2\text{D}} - E_{2\text{D}+\text{S}}}{N_{2\text{D}}}, \quad (1)$$

where $E_{2\text{D}+\text{S}}$ is the energy of the strained 2D III-V material adsorbed on the surface of substrate, E_{S} is the energy of the substrate slab, $E_{2\text{D}}$ is the energy of the isolated unstrained 2D III-V materials, and $N_{2\text{D}}$ is the number of atoms in the unit cell of the 2D materials, which is two for the hexagonal structures and four for the tetragonal ones. The binding energy of the 2D materials on the substrates is calculated in two ways, using the PBE functional as well as using the vdW-DF functional with an optB88 exchange functional to include the effect of van der Waals interactions [21].

Figures 4(c) and 4(d) show the formation energies $E_{\text{vac}}^{\text{f}}$ of the isolated unstrained 2D materials with respect to their 3D structures as red open symbols and the reduced formation energies for the strained 2D materials adsorbed on the substrates, $E_{\text{ads}}^{\text{f}} = E_{\text{vac}}^{\text{f}} - E_{\text{b}}$. The black symbols correspond to the formation energies $E_{\text{ads,PBE}}^{\text{f}}$, obtained from the PBE adsorption

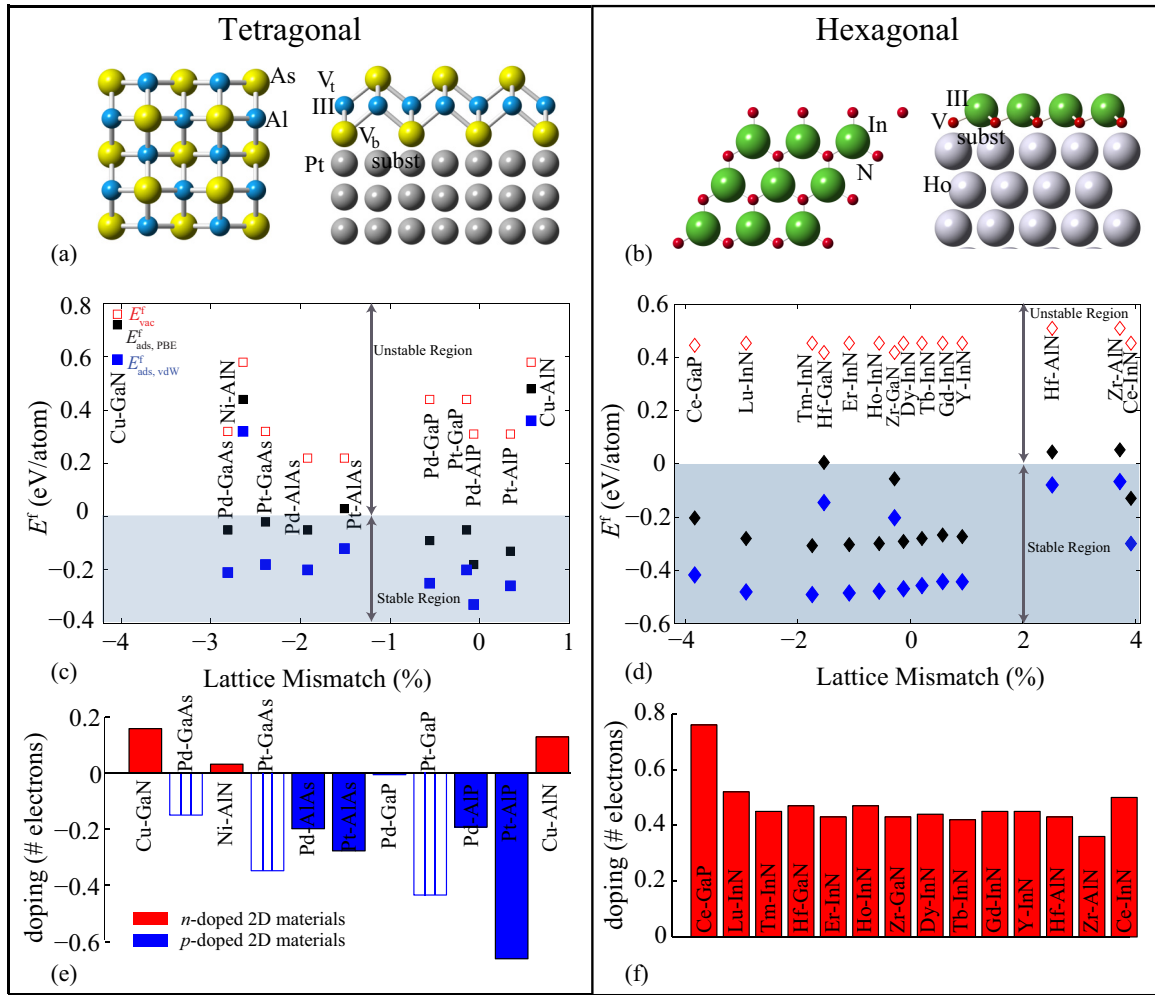


FIG. 4. (Color online) (a) Top and side views of isolated 2D tetragonal AIAs and adsorbed on Pt(100). (b) Top and side views of isolated 2D hexagonal InN and adsorbed on Ho(0001) surface. The formation energies are shown for various combinations of substrates and 2D materials with lattice mismatches up to 4% for (c) the tetragonal and (d) the hexagonal structures. Formation energies of the 2D III-V materials relative to their 3D bulk phases for the isolated unstrained 2D materials E_{vac}^f (red), the strained 2D materials absorbed on the substrates as calculated using the PBE functional neglecting van der Waals interactions $E_{\text{ads,PBE}}^f$ (black symbols), and as calculated using the vdW-DF functional that includes van der Waals interactions $E_{\text{ads,vdW}}^f$ (blue symbols). The shaded region shows the regime where 2D materials are stable on these substrates. Electrons transferred from substrate surface atoms to the 2D materials, a measure of the doping of the 2D materials, for (e) tetragonal 2D materials adsorbed on fcc transition metals, and (f) hexagonal 2D materials on hcp transition and rare-earth metals. Red bars denote electrons lost from the substrate surface atoms, filled blue bars show electrons gained by the substrate for semiconducting hexagonal and tetragonal 2D materials, and open blue bars show electrons gained by substrate surface atoms for metallic tetragonal 2D materials.

energies, which neglect the van der Waals interactions. The blue symbols correspond to the formation energies $E_{\text{ads,vdW}}^f$, obtained using the vdW-DF functional that includes van der Waals interactions. The reduced formation energies of the 2D materials on the substrates are a measure of the energy released upon adsorbing a layer of the 2D III-V material detached from a bulk 3D phase onto the substrate. These energies include the cost of straining the 2D materials. As an example, for AIAs the formation energy of the isolated 2D material of $E_f^f = 0.22$ eV/atom is reduced by the adsorption on Pt to $E_{\text{ads,vdW}}^f = -0.12$ eV/atom, stabilizing this 2D material.

The successful synthesis of a 2D material on a particular substrate should be feasible when the formation energy of the 2D material on that substrate becomes negative. The regime of stable 2D materials on substrates, i.e., negative formation energies, is shaded in blue in Figs. 4(c) and 4(d)

(see Supplemental Material [29] for the values of the formation energies and structural details for the 2D materials adsorbed on the substrates).

Figure 4(c) shows the formation energies for the tetragonal 2D materials adsorbed on the transition-metal substrates. First, we find that unlike graphene, which is only weakly physisorbed on transition-metal substrates [32–34], the adsorption of the tetragonal III-V materials on the transition-metal surfaces is dominated by the chemical and electrostatic interactions as described by the PBE functional. This is due to the polar nature of the III-V materials. Second, we observe that the adsorption energy reduces with the filling of the d shell of the transition-metal substrates. Finally, for all 2D tetragonal materials considered in this study, other than AlN and GaN, we identify suitable transition-metal substrates that stabilize these 2D materials. In contrast to the other tetragonal materials,

AlN and GaN are found to interact more strongly with the substrates in the top(III)-hollow(V) configuration due to the large electronegativity difference between the substrate atoms and group-V atoms. In other words, the top site is preferentially occupied by the atom whose electronegativity is similar to that of the substrate atoms.

Likewise, Fig. 4(d) shows the formation energies for the 2D hexagonal materials adsorbed on hcp transition-metal and rare-earth-metal substrates. We find that all these 2D materials exhibit negative formation energies when adsorbed on these substrates. On adsorption on the rare-earth-metal substrates, all 2D hexagonal materials buckle or increase their buckling with the group-V atoms preferentially facing the rare-earth-metal substrates. The buckling of the adsorbed materials is predominantly caused by the chemical interaction of the 2D materials with the substrates. AlN and GaN on adsorption on the Hf and Zr substrates also buckle, however, the group-III element faces the transition-metal substrate. On the rare-earth substrates, the ionicity of the 2D materials increases, while it decreases on the transition-metal substrates. Overall, the negative formation energy implies that we can stabilize and synthesize the 2D hexagonal materials on these substrates. In addition, for 2D hexagonal InN, we have identified eight rare-earth-metal substrates with lattice mismatches ranging from -3% to $+1\%$. This may enable the study of different substrates and strains to tune the electronic properties such as doping level of these 2D materials, which will be discussed in the following.

To determine if the range of calculated formation energies for the 2D III-V materials on the substrates is sufficient to stabilize the materials under experimental growth conditions, we compare the results with calculations for 2D materials that have successfully been synthesized on substrates, such as graphene on Cu(111) and Pt(111) [4], MoS₂ on SiO₂ [35], and BN on Cu(111) and Ni(111) [36,37]. Among these, the formation energy of graphene is about 53 meV/atom [38] with comparable binding energies that range from 30 meV/atom [34] to 183 meV/atom [39] on several transition-metal surfaces. Epitaxially adsorbed BN on Cu(111) and Ni(111) surfaces exhibits adsorption energies of up to 135 meV/atom [40] while its formation energy is only about 50 meV/atom [38]. The formation energy of MoS₂ in its hexagonal layered 2H structure is 60 meV/atom [41] and the binding energies on Ir(111), Pd(111), and Ru(0001) surfaces are up to 330 meV/atom [42]. Using these values, we find that the formation energies of these 2D materials on the various substrates range from $+0.02$ to -0.13 eV/atom for graphene, to -0.08 eV/atom for BN, to -0.27 eV/atom for MoS₂. These values are comparable to our predicted formation energies of the 2D III-V tetragonal and hexagonal materials on the transition-metal substrates which range from -0.33 to -0.07 eV/atom, excluding tetragonal AlN and GaN. More recently [43], submonolayer to 12-monolayer graphite like AlN nanosheets were grown on Ag(111) single crystals using molecular beam epitaxy, motivating the possibility of growth of hexagonal AlN from the bulk wurtzite AlN structure by assistance of a suitable substrates. The similarities of the formation energies of these successfully synthesized 2D materials on substrates and our predictions indicate that the transition-metal substrates we identified will sufficiently stabilize these novel 2D III-V materials.

In comparison to the formation energies of the 2D tetragonal and hexagonal materials on the transition-metal substrates, the values for the 2D hexagonal materials adsorbed on hcp rare-earth metals are significantly lower, ranging from -0.3 to -0.5 eV/atom. As a consequence, even though the 2D hexagonal materials GaP, InN, and GaN will be stabilized, they may be difficult to transfer to other substrates following their growth.

C. Nature of 2D material substrate interaction

To make a quantitative assessment of the type of bonding present between the 2D materials and the substrates, we estimate the charge transfer occurring during adsorption. Figures 4(e) and 4(f) show the electron transfer from the substrates to the 2D III-V materials computed using the Bader formalism [44] (the values are listed in the Supplemental Material [29]). The charge transfer results in doping of the 2D materials. Adsorbed tetragonal AlN and GaN and hexagonal AlN, GaN, GaP, and InN are *n*-type doped, whereas tetragonal AlAs, AlP, GaP, and GaAs are *p*-type doped.

The charge transfer for the 2D tetragonal materials adsorbed on the fcc transition-metal substrates varies from -0.66 to $+0.16$ electrons per atom of the 2D material, resulting mostly in *p*-doped 2D tetragonal materials. In contrast, the charge transfer for the 2D hexagonal materials adsorbed on hcp transition- and rare-earth-metal substrates is larger and ranges from $+0.36$ to $+0.76$, leading to *n*-type doping of the 2D hexagonal materials. The larger charge transfer for the 2D hexagonal materials compared to the 2D tetragonal ones correlates with stronger binding energies. Furthermore, the binding energy of the 2D hexagonal materials is larger for the hcp rare-earth-metal substrates than the transition-metal substrates. The binding energy for the 2D tetragonal materials on the fcc transition-metal substrates ranges from 0.17 to 0.69 eV/atom, for the 2D hexagonal materials on hcp transition-metal substrates from 0.56 to 0.62 eV/atom, and for the 2D hexagonal materials on rare-earth-metal substrates from 0.75 to 0.94 eV/atom.

The charge transfer is reflected in the changes of the charge-density distribution shown in Fig. 5 for 2D tetragonal AlAs and hexagonal InN adsorbed on Pt(100) and Ho(0001) substrates, respectively. The charge density for isolated AlAs in Fig. 5(a) shows a significant charge transfer of about 2 electrons from Al to As, which is characteristic of the ionic bonding between Al and As and a consequence of the electronegativity difference between these elements. The ionic nature of the bonding between Al and As is retained when the 2D material is adsorbed on Pt. In addition, a charge transfer of 0.28 electrons from the bottom As atom to the Pt surface is observed in the Bader charge analysis. As can be seen in Figs. 5(b) and 5(c), some charge accumulates in the region between the As and Pt surface atoms and some is transferred to the Pt surface atoms, indicating the formation of a covalent bond. This bonding results from the overlap of the *p* orbitals of the group-V atoms with the *d* orbitals of the transition-metal atoms. Similarly, the analysis of the charge-density distribution of the 2D hexagonal InN on Ho in Figs. 5(d)–5(f) reveals orbital overlap between the 2D material and substrate atoms. The transferred charge of 0.5 electrons from the Ho substrate

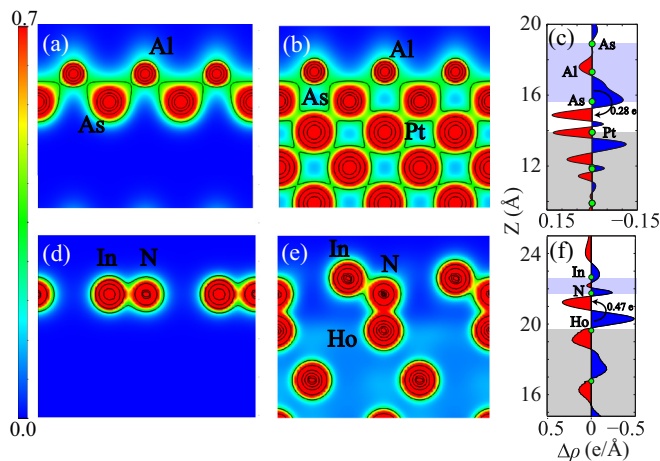


FIG. 5. (Color online) Charge densities distribution for (a) isolated tetragonal AlAs, (b) tetragonal AlAs adsorbed on Pt(100), (d) isolated hexagonal InN, and (e) hexagonal InN adsorbed on Ho(0001). The cross section for AlAs is taken along the (100) plane passing through the As atoms closest to Pd and for InN it is taken along the $(\bar{1}10)$ plane. The charge density is in units of electrons/ \AA^3 . Plots of the plane-averaged electron density difference $\Delta\rho$ between the interacting and isolated 2D material and substrate pair along the direction perpendicular to the interface for the fixed geometry of the adsorbed case are shown in (c) for AlAs on Pt and (f) for InN on Ho. The red and blue colors indicate electron accumulation and depletion, respectively.

to the 2D hexagonal InN is localized on the N atom, leading to the formation of a partly ionic bond between the N and Ho atoms and a buckling of the 2D hexagonal InN structure.

The equilibrium spacing between the bottom group III/V atoms of the 2D materials and the substrate surface atoms ranges from 2.0 to 2.6 \AA . This is consistent with the formation of a chemical bond as seen in the charge density and is different than in the case of graphene on transition metals where weak van der Waals interactions lead to a larger separation of 3.3 \AA [34]. The vdW-DF functional only slightly alters the adsorption distances of the 2D III-V materials (see Supplemental Material [29] for comparison of adsorption distances obtained from PBE and vdW-DF functional calculations). All of the planar hexagonal 2D materials buckle upon adsorption. The buckling is a consequence of the balance between the attraction and repulsion of the group-III and -V atoms with the substrates. Also, buckled tetragonal and hexagonal materials retain their buckling with a change of a few percent to accommodate the effect of strains and chemical bonding with the substrate. MoS_2 on transition-metal substrates [42], silicene on Ag(111) substrate [45], silicene on ZrB_2 (0001) substrate [46], and BN on Ni(111) and Cu(111) substrates [30] exhibit similar spacings between the 2D materials and the substrates. Moreover, varying buckling of the 2D materials, depending on the system under consideration, has also been observed in the aforementioned studies.

Overall, the substrates in this work, particularly the fcc and hcp transition metals, are ideal for the synthesis of these 2D III-V materials as they provide strong energetic stabilization as well as minimal distortion of the geometry of these 2D materials.

D. Electronic properties of 2D materials on substrates

The presence of the substrates can alter the electronic structure of the 2D III-V materials, which ranges from metallic to semiconducting with direct and indirect band gaps. Among the 2D materials studied in this work, the semiconductors include hexagonal AlN, GaN, InN, and GaP and tetragonal AlN, GaN, AlP, and AlAs. The tetragonal GaP and GaAs systems are metals. The change in the electronic structure when the 2D materials are epitaxially adsorbed on the metal substrates is due to strain, charge transfer, and chemical interactions. We first determine how strain affects the electronic structure of the isolated 2D materials and then show how the adsorption of the 2D materials on the metal substrates modifies the electronic structure and results in doping of the 2D materials.

Application of strain is a well-known approach in the field of electronic device design for tuning the electronic properties of semiconductors [47] and can also be applied to 2D materials [9]. Figure 6(a) shows the dependence of the band gap on applied biaxial strain for isolated 2D tetragonal AlN and AlP and 2D hexagonal GaSb and InN. We find that the band gap decreases nearly linearly upon application of tensile biaxial strain for all these systems. This is different to the 2D hexagonal boron pnictides, where the band gap increases under biaxial tensile strain for BP, BAs, and BSb and decreases for BN [9].

Next, we determine how the adsorption of the 2D materials on the metal substrates affects their electronic structure using the Bader charge analysis and the electronic density of states. Figure 6(b) shows the density of states of isolated hexagonal InN under 0.56% compressive strain to match the lattice parameter of the Ho substrate (black dotted line), and adsorbed on the Ho(0001) substrate (red line). The density of states of isolated hexagonal InN is shifted by -1.68 eV to overlay on the density of states of adsorbed InN. First, we observe that the band gap of the isolated InN increases upon application of compressive biaxial strain similar to the other 2D materials shown in Fig. 6(a). This can also be verified by comparing the density of states of strained and unstrained isolated InN shown in the Supplemental Material [29]. Second, we find that the density of states of 2D hexagonal InN upon adsorption on Ho shifts to lower energies by about 1.68 eV and the material becomes metallic.

To support this observation, we calculate the band structure projected onto specific atomic sites, the so-called “fat bands.” Figure 7 shows the site-projected band structure for single-layer InN, AlN, and AlAs freestanding and adsorbed onto Ho, Ni, and Pt, respectively. The symbol sizes and colors are proportional to the sum of the weights of the orthonormal orbitals at a particular site. In Fig. 7(a), N and In sites contribute equally to the InN bands near the valence band maximum (VBM). The electronic band structure of InN adsorbed on Ho in Figs. 7(b) and 7(c) shows that some bands remain dominated by N and In contributions when InN is adsorbed on Ho.

The larger contributions come from the intrinsic bands of InN while smaller contributions are the result of strong bonding of the metallic Ho substrate surface with semiconducting InN. Comparison of Fig. 7(a) to Figs. 7(b) and 7(c) shows that the Fermi level is shifted relative to the vacuum level when InN is adsorbed on the substrate, as emphasized by an arrow

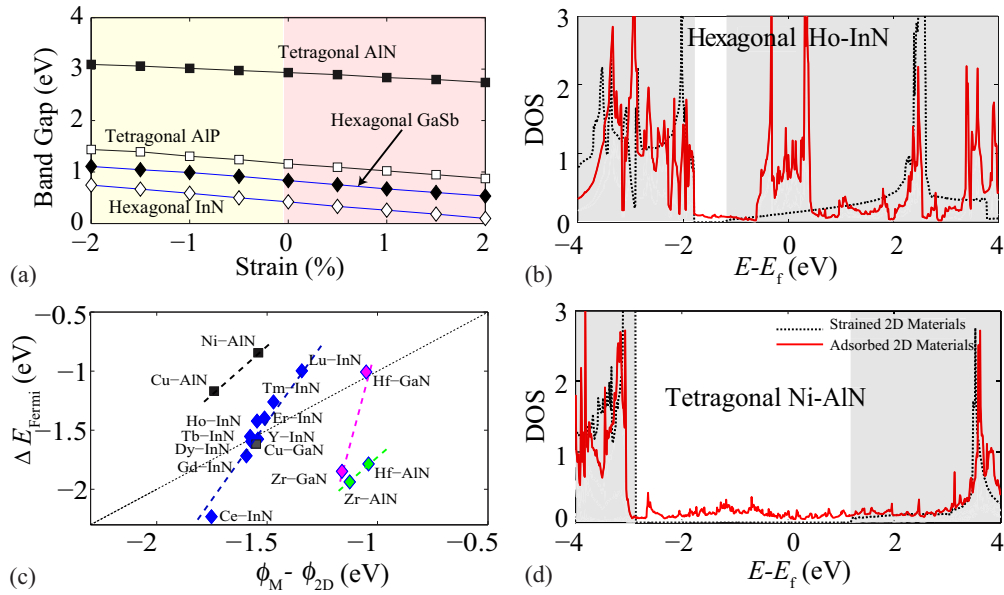


FIG. 6. (Color online) (a) Strain effect on the band gap of 2D tetragonal AlN, AlP, hexagonal GaSb, and InN. Positive strains refer to biaxial tensile and negative to biaxial compressive strains. (b) Shifted density of states of strained 2D III-V material in vacuum (black dotted line), and unshifted density of states of 2D III-V material adsorbed on substrate (red solid line) for hexagonal InN on Ho(0001) and (d) for tetragonal AlN on Ni(100). The density of states has the units of states per eV per unit cell of 2D material. The shaded gray region corresponds to the conduction and valence band regions of the strained 2D material. (c) Shift in Fermi level of the 2D material ΔE_{Fermi} versus the work function difference between the metals and 2D materials $\phi_M - \phi_{2D}$. Square symbols indicate the 2D tetragonal materials and diamonds the hexagonal ones.

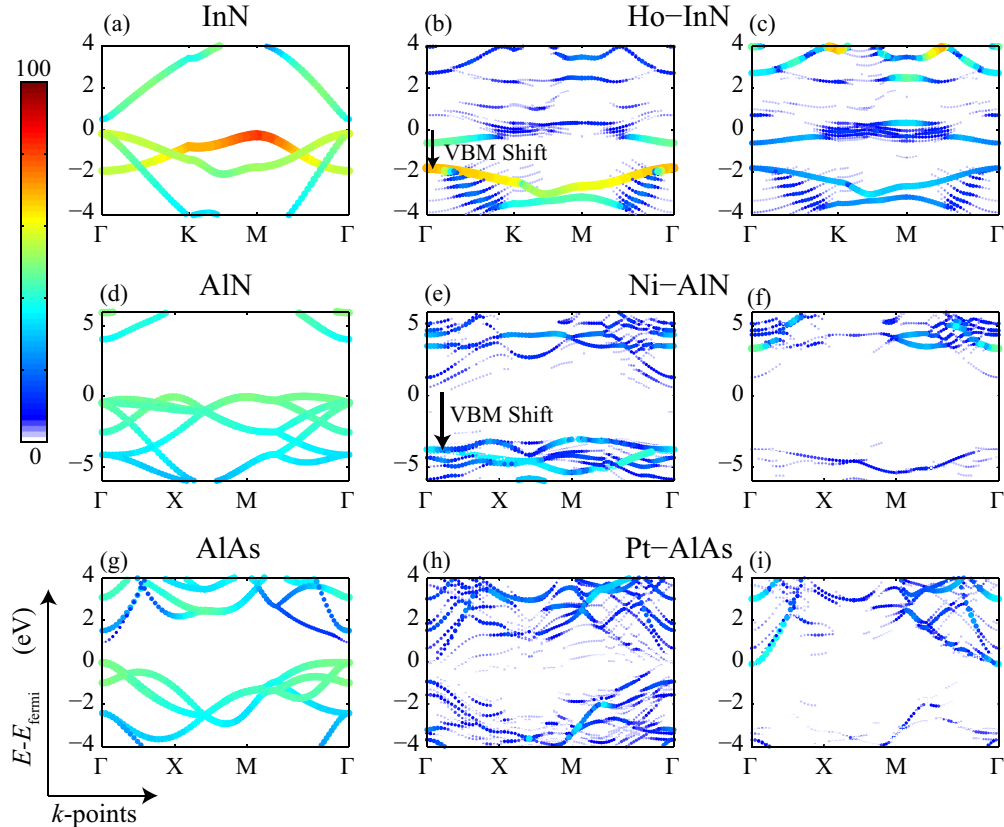


FIG. 7. (Color online) Electronic band structure projected on group-V atoms of (a) InN, (b) InN on Ho(0001), (d) AlN, (e) AlN on Ni(100), (g) AlAs, and (h) AlAs on Pt(100). Band structure projected on group-III atoms of (c) InN on Ho(0001), (f) AlN on Ni(100), and (i) AlAs on Pt(100). The valence band maximum is set to zero. The symbol sizes and colors denote the weights of the specific site.

in Fig. 7(b). In addition, the change from semiconducting to metallic nature in InN before and after adsorption can be clearly seen in the band structure. The shift of the Fermi level is due to the charge transfer of about 0.5 electrons from the metal substrate to the 2D material [see Fig. 4(f)], resulting in strong *n*-type doping of 0.25 electrons per atom of the 2D hexagonal InN.

The charge transfer from the substrates to the 2D materials is caused by the differences in the work functions between the 2D materials ϕ_{2D} and the metal substrates ϕ_M . When the 2D materials interact with the metal substrates, electrons are transferred from the material with the lower work function to the one with the higher work function to reduce the energy. For a rigid band model, one would expect that 2D materials are doped with electrons if $\phi_M < \phi_{2D}$ [32].

We study all combinations of substrates and 2D hexagonal materials and find *n*-type doping with a Fermi level shift ΔE_{Fermi} that is correlated to the difference in work function as shown in Fig. 6(c). The work functions of the 2D materials and substrates are given by the difference of their electrostatic potential in the vacuum and their VBM. An estimate of the Fermi level shifts are made by analyzing the integrated local density of states of the 2D materials isolated and adsorbed on the substrates and then identifying the region where the integrated density of states shows a plateau with a similar integrated electron count (see Supplemental Material [29] for density of states of isolated 2D materials and 2D materials adsorbed on substrates). The Fermi level shift is taken as the sum of the shift in the VBM of the adsorbed 2D material with respect to the Fermi level of the combined 2D materials and substrate and half the band-gap energy of the strained isolated 2D materials. The results for 2D hexagonal InN on nine different substrates show that for a given 2D material, the Fermi level shift depends nearly linearly on the difference between the work function of the metal substrate and the 2D material $\phi_M - \phi_{2D}$, as shown in Fig. 6(c). Furthermore, for a given difference in work function, the Fermi level shift depends strongly on the specific 2D III-V material. For example, for the same $\phi_M - \phi_{2D} \approx -1.15$ eV, the magnitude of Fermi level shift is in the order $\text{InN} > \text{GaN} > \text{AlN}$. These results demonstrate that the doping of the 2D materials can be controlled by the choice of substrate.

Figure 6(d) illustrates using the density of states that the presence of the Ni substrate shifts the Fermi level of tetragonal AlN. The density of states of isolated-strained AlN is shifted

by an equivalent of the Fermi level shift, estimated as discussed above, for an easy comparison to the density of states of AlN adsorbed on Ni. The Fermi level shift is further corroborated by comparing Figs. 7(d) and 7(e) and 7(f) where N states are found to shift about 4 eV upon adsorption of AlN on the Ni substrate. It is apparent from the density of states and electronic band structure that AlN becomes metallic on adsorption on Ni and is also *n*-type doped. Similarly, we studied the density of states for all other pairs of tetragonal 2D materials on substrates (see Supplemental Material [29]). All semiconducting tetragonal 2D materials become metallic and all metallic tetragonal 2D materials remain metallic upon adsorption on a substrate. However, Fermi level shifts are identifiable only for the cases of Ni-AlN, Cu-AlN, and Cu-GaN as the densities of states of only these adsorbed 2D materials are similar to the one of the isolated 2D material. For example, Fig. 7(h) shows that the bands of AlAs are heavily modified when it is adsorbed on the (100) surface of Pt, making the intrinsic bands of isolated semiconducting AlAs [Fig. 7(g)] unidentifiable. Discernible Fermi level shifts are plotted against the $\phi_M - \phi_{2D}$ in Fig. 6(c) as squares. These combinations of substrates and tetragonal materials result in *n*-type doping of the 2D materials. Furthermore, the Fermi level shifts are in accordance with a first-order rigid band shift model for work functions. In the case of AlAs and AlP adsorbed on Pt and Pd, the substrates lead to *p*-type doping of the 2D materials.

Figure 8 shows the work functions of the 2D tetragonal and hexagonal materials as a function of their empirical Mulliken electronegativity, where the electronegativity of the 2D materials is obtained from the geometric mean of the atomic Mulliken electronegativities [48]. While for metals, the electronegativities agree well with the work functions, deviations occur for binary compounds, which depend on the valence state of the atoms and band gap of the materials [48,49]. We observe similar deviations for the 2D materials and find a significant difference for the work function between the tetragonal and hexagonal 2D materials with the majority of tetragonal materials having a larger work function. The difference between the electronegativities and work functions for the two structures is not surprising because the nature of the bonding in the two structures is notably different [8]. While the electronegativities can not quantitatively predict the work function of these 2D materials, they explain the trend for each of the families of tetragonal and hexagonal 2D structures; the work function and electronegativity decrease

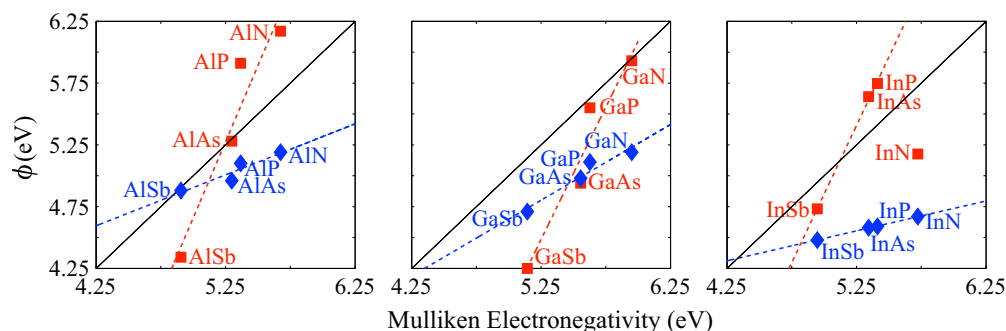


FIG. 8. (Color online) Work function of 2D III-V hexagonal materials, diamond symbols, and 2D III-V tetragonal materials, square symbols compared to their Mulliken electronegativities.

monotonically along the sequence going from N to Sb compounds and Al to In. The only exception is tetragonal InN, possibly due to the strong energetic preference of hexagonal InN. Taking into account the band gaps and the valence states of the group-III and -V atoms in the 2D materials by modifying the Mulliken electronegativities [50] does not improve the correlations shown in Fig. 8 (see Supplemental Material [29]).

We digress from questions of synthesis to studying the work function of these 2D materials as it is an important parameter in the design of solid-state electronics and photocathodes. For instance, the (100) surface of bulk GaAs is widely used as a photocathode. Its work function is 5.5–5.6 eV, depending on the surface reconstructions [51]. We predict for GaAs that the work function is reduced by about 0.6 eV when going from the bulk phase to the 2D tetragonal and hexagonal structures. Knowledge of work function of the 2D materials may facilitate their use as photoemitters or in related applications.

V. CONCLUSION

We identified several transition-metal and rare-earth-metal substrates that can be used to synthesize and stabilize the recently predicted metastable family of 2D hexagonal and tetragonal III-V materials. The reduced elastic constants of

the 2D III-V materials and their strong adsorption on the metal substrates enable the epitaxial stabilization of these materials with strains of up to 4%. We show that the substrates alter the electronic properties of these 2D materials through epitaxial strain, formation of chemical bonds, and doping. The difference in work functions between the 2D materials and the metal substrates leads to doping of the 2D materials. The large adsorption energies and strong doping indicate that these metals should provide good electrical contact for transport measurements and electronic applications. We expect these results will provide helpful guidance to synthesis experiments, materials design, and application of these 2D materials.

ACKNOWLEDGMENTS

The authors thank K. Mathew and M. Johannes for helpful discussions. The work was supported by the NSF CAREER Award No. DMR-1056587 and through the Cornell Center for Materials Research under Award No. DMR-1120296. The research used computational resources of the Texas Advanced Computing Center under Contract No. TG-DMR050028N and of the Computation Center for Nanotechnology Innovation at Rensselaer Polytechnic Institute.

-
- [1] K. S. Novoselov, A. K. Geim, S. V. Morozov, D. Jiang, Y. Zhang, S. V. Dubonos, I. V. Grigorieva, and A. A. Firsov, *Science* **306**, 666 (2004).
- [2] K. S. Novoselov, D. Jiang, F. Schedin, T. J. Booth, V. V. Khotkevich, S. V. Morozov, and A. K. Geim, *Proc. Natl. Acad. Sci. U. S. A.* **102**, 10451 (2005).
- [3] K. S. Novoselov, *Rev. Mod. Phys.* **83**, 837 (2011).
- [4] K. S. Novoselov, V. Falco, L. Colombo, P. R. Gellert, M. G. Schwab, and K. Kim, *Nature (London)* **490**, 192 (2012).
- [5] K. F. Mak, C. Lee, J. Hone, J. Shan, and T. F. Heinz, *Phys. Rev. Lett.* **105**, 136805 (2010).
- [6] C. Tusche, H. L. Meyerheim, and J. Kirschner, *Phys. Rev. Lett.* **99**, 026102 (2007).
- [7] C. Jin, F. Lin, K. Suenaga, and S. Iijima, *Phys. Rev. Lett.* **102**, 195505 (2009).
- [8] H. L. Zhuang, A. K. Singh, and R. G. Hennig, *Phys. Rev. B* **87**, 165415 (2013).
- [9] H. L. Zhuang and R. G. Hennig, *Appl. Phys. Lett.* **101**, 153109 (2012).
- [10] H. L. Zhuang and R. G. Hennig, *Chem. Mater.* **25**, 3232 (2013).
- [11] S. Lebègue, T. Björkman, M. Klintonberg, R. M. Nieminen, and O. Eriksson, *Phys. Rev. X* **3**, 031002 (2013).
- [12] H. Zhong, G. Yang, H. Song, Q. Liao, H. Cui, P. Shen, and C.-X. Wang, *J. Phys. Chem. C* **116**, 9319 (2012).
- [13] H. Fang, S. Chuang, T. C. Chang, K. Takei, T. Takahashi, and A. Javey, *Nano Lett.* **12**, 3788 (2012).
- [14] J. M. Garcia, U. Wurstbauer, A. Levy, L. N. Pfeiffer, A. Pinczuk, A. S. Plaut, L. Wang, C. R. Dean, R. Buizza, A. M. V. D. Zande, J. Hone, K. Watanabe, and T. Taniguchi, *Solid State Commun.* **152**, 975 (2012).
- [15] J. Hwang, D. Campbell, S. Shivaraman, H. Alsalman, J. Y. Kwak, M. Kim, A. R. Woll, A. Singh, R. G. Hennig, S. Gorantla, M. H. Rummeli, and M. G. Spencer, *ACS Nano* **7**, 385 (2013).
- [16] Y. H. Lee, X. Q. Zhang, W. Zhang, M. T. Chang, C. T. Lin, K. D. Chang, Y. C. Yu, J. T. W. Wang, C. S. Chang, L. J. Li, and T. W. Lin, *Adv. Mater.* **24**, 2320 (2012).
- [17] Y. Shi, C. Hamsen, X. Jia, K. K. Kim, A. Reina, M. Hofmann, A. L. Hsu, K. Zhang, H. Li, Z.-Y. Juang, M. S. Dresselhaus, L.-J. Li, and J. Kong, *Nano Lett.* **10**, 4134 (2010).
- [18] G. Kresse and J. Furthmüller, *Phys. Rev. B* **54**, 11169 (1996).
- [19] P. E. Blöchl, *Phys. Rev. B* **50**, 17953 (1994).
- [20] G. Kresse and D. Joubert, *Phys. Rev. B* **59**, 1758 (1999).
- [21] J. Klimeš, D. R. Bowler, and A. Michaelides, *Phys. Rev. B* **83**, 195131 (2011).
- [22] P. Havu, V. Blum, V. Havu, P. Rinke, and M. Scheffler, *Phys. Rev. B* **82**, 161418 (2010).
- [23] P. Gardner, M. Tüshaus, R. Martin, and A. Bradshaw, *Surf. Sci.* **240**, 112 (1990).
- [24] A. Borg, A.-M. Hilmen, and E. Bergene, *Surf. Sci.* **306**, 10 (1994).
- [25] M. Ronning, E. Bergene, A. Borg, S. Aussen, and A. Holmen, *Surf. Sci.* **477**, 191 (2001).
- [26] L. Nilsson, M. Andersen, R. Balog, E. Lægsgaard, P. Hofmann, F. Besenbacher, B. Hammer, I. Stensgaard, and L. Hornekær, *ACS Nano* **6**, 10258 (2012).

- [27] C. Soldano, A. Mahmood, and E. Dujardin, *Carbon* **48**, 2127 (2010).
- [28] G. Bergerhoff and I. D. Brown, *Crystallographic Databases* (International Union of Crystallography, Chester, 1987).
- [29] See Supplemental Material at <http://link.aps.org/supplemental/10.1103/PhysRevB.89.245431> for detailed information about the structures, elastic constants, energies, and electronic properties of the 2D materials free standing and adsorbed on the substrates.
- [30] R. Laskowski, P. Blaha, and K. Schwarz, *Phys. Rev. B* **78**, 045409 (2008).
- [31] N. Joshi and P. Ghosh, *Phys. Rev. B* **87**, 235440 (2013).
- [32] G. Giovannetti, P. A. Khomyakov, G. Brocks, V. M. Karpan, J. van den Brink, and P. J. Kelly, *Phys. Rev. Lett.* **101**, 026803 (2008).
- [33] M. Fuentes-Cabrera, M. I. Baskes, A. V. Melechko, and M. L. Simpson, *Phys. Rev. B* **77**, 035405 (2008).
- [34] M. Vanin, J. J. Mortensen, A. K. Kelkkanen, J. M. Garcia-Lastra, K. S. Thygesen, and K. W. Jacobsen, *Phys. Rev. B* **81**, 081408 (2010).
- [35] A. M. van der Zande, P. Y. Huang, D. A. Chenet, T. C. Berkelbach, Y. You, G.-H. Lee, T. F. Heinz, D. R. Reichman, D. A. Muller, and J. C. Hone, *Nat. Mater.* **12**, 554 (2013).
- [36] A. Preobrajenski, A. Vinogradov, and N. Mårtensson, *Surf. Sci.* **582**, 21 (2005).
- [37] K. K. Kim, A. Hsu, X. Jia, S. M. Kim, Y. Shi, M. Hofmann, D. Nezich, J. F. Rodriguez-Nieva, M. Dresselhaus, T. Palacios, and J. Kong, *Nano Lett.* **12**, 161 (2012).
- [38] G. Graziano, J. Klimeš, F. Fernandez-Alonso, and A. Michaelides, *J. Phys.: Condens. Matter* **24**, 424216 (2012).
- [39] I. Hamada and M. Otani, *Phys. Rev. B* **82**, 153412 (2010).
- [40] S. Joshi, D. Eciija, R. Koitz, M. Iannuzzi, A. P. Seitsonen, J. Hutter, H. Sachdev, S. Vijayaraghavan, F. Bischoff, K. Seufert, J. V. Barth, and W. Auwärter, *Nano Lett.* **12**, 5821 (2012).
- [41] H. Rydberg, M. Dion, N. Jacobson, E. Schröder, P. Hyldgaard, S. I. Simak, D. C. Langreth, and B. I. Lundqvist, *Phys. Rev. Lett.* **91**, 126402 (2003).
- [42] W. Chen, E. J. Santos, W. Zhu, E. Kaxiras, and Z. Zhang, *Nano Lett.* **13**, 509 (2013).
- [43] P. Tsipas, S. Kassavetis, D. Tsoutsou, E. Xenogiannopoulou, E. Goliias, S. A. Giamini, C. Grazianetti, D. Chiappe, A. Molle, M. Fanciulli, and A. Dimoulas, *Appl. Phys. Lett.* **103**, 251605 (2013).
- [44] W. Tang, E. Sanville, and G. Henkelman, *J. Phys.: Condens. Matter* **21**, 084204 (2009).
- [45] H. Enriquez, S. Vizzini, A. Kara, B. Lalmi, and H. Oughaddou, *J. Phys.: Condens. Matter* **24**, 314211 (2012).
- [46] C.-C. Lee, A. Fleurence, R. Friedlein, Y. Yamada-Takamura, and T. Ozaki, *Phys. Rev. B* **88**, 165404 (2013).
- [47] T. K. S. Wong, *Semiconductor Strain Metrology Principles and Applications* (Bentham Science, Sharjah, 2012).
- [48] E. C. M. Chen, W. E. Wentworth, and J. A. Ayala, *J. Chem. Phys.* **67**, 2642 (1977).
- [49] S. G. Bratsch, *J. Chem. Ed.* **65**, 34 (1988).
- [50] K. F. Purcell and J. C. Kotz, *An Introduction to Inorganic Chemistry* (Saunders College, Philadelphia, 1980).
- [51] S. Kul'kova, S. Eremeev, A. Postnikov, and I. Shein, *J. Exp. Theor. Phys.* **104**, 590 (2007).